A Model Approach to Uncover the Role of the IrOx Crystallographic Structure and Chemistry on OER Activity and Stability via Annealing a Sacrificial Template

Delphine Clauss, Vincent Martin, Jaysen Nelayah, Raphaël Chattot, Pierre Bordet, Jakub Drnec, Marta Mirolo, Laetitia Dubau, Frédéric Maillard

A Model Approach to Uncover the Role of the IrO_x Crystallographic Structure and Chemistry on OER Activity and Stability via Annealing a Sacrificial Template

Delphine Clauss*[a], Vincent Martin[a], Jaysen Nelayah[b], Raphaël Chattot[c], Pierre Bordet[d], Jakub Drnec[e], Marta Mirolo[e], Laetitia Dubau[a], Frédéric Maillard*[a]

[a]*Univ. Grenoble Alpes, Univ. Savoie-Mont-Blanc, CNRS, Grenoble-INP, LEPMI, 38000 Grenoble, France*, *1130 Rue de la Piscine, 38610 38402 Saint Martin d'Hères, France*

[b]*Laboratoire Matériaux et Phénomènes Quantiques, Université Paris Cité - CNRS, 75013 Paris, France*

[c]*ICGM, Univ. Montpellier, CNRS, ENSCM, 34095 Montpellier cedex 5, France*

[d]*CNRS, Institut Néel, F-38000 Grenoble, France*

[e]*ESRF, The European Synchrotron, 71 Avenue des Martyrs, CS40220, 38043 Grenoble Cedex 9, France*

KEYWORDS: Proton-Exchange Membrane Water Electrolysis, Oxygen Evolution Reaction, Iridium Oxide, Thermal annealing, Nanoparticles.

ABSTRACT

Iridium oxide nanoparticles (IrO_x NPs) hold promise to lower the catalyst cost of proton-exchange membrane water electrolyzers (PEMWE). However, their enhanced oxygen evolution reaction (OER) activity often comes at the expense of stability. Achieving a delicate balance between these two conflicting properties requires a comprehensive understanding of how the structural, morphological, and chemical characteristics of IrO_x NPs influence them. To address this challenge, we synthesized IrO_x NPs supported on carbon (IrO_x/C), and annealed them in air at temperatures ranging from 340°C to 870°C. We obtained a library of materials, ranging from small, amorphous IrO_x NPs supported on carbon to larger self-supported crystalline IrO_2. Using this library, we evidence the critical role of the IrO_x particle size, crystallinity and chemistry on both the OER activity and catalyst stability. We further identify that an annealing temperature of 520°C provides an optimal balance between OER activity and stability, and we demonstrate size control of unsupported small IrO_2 NPs at temperatures above 500°C, highlighting the significant role of the sacrificial support in shaping nano-structured IrO_2 catalysts.

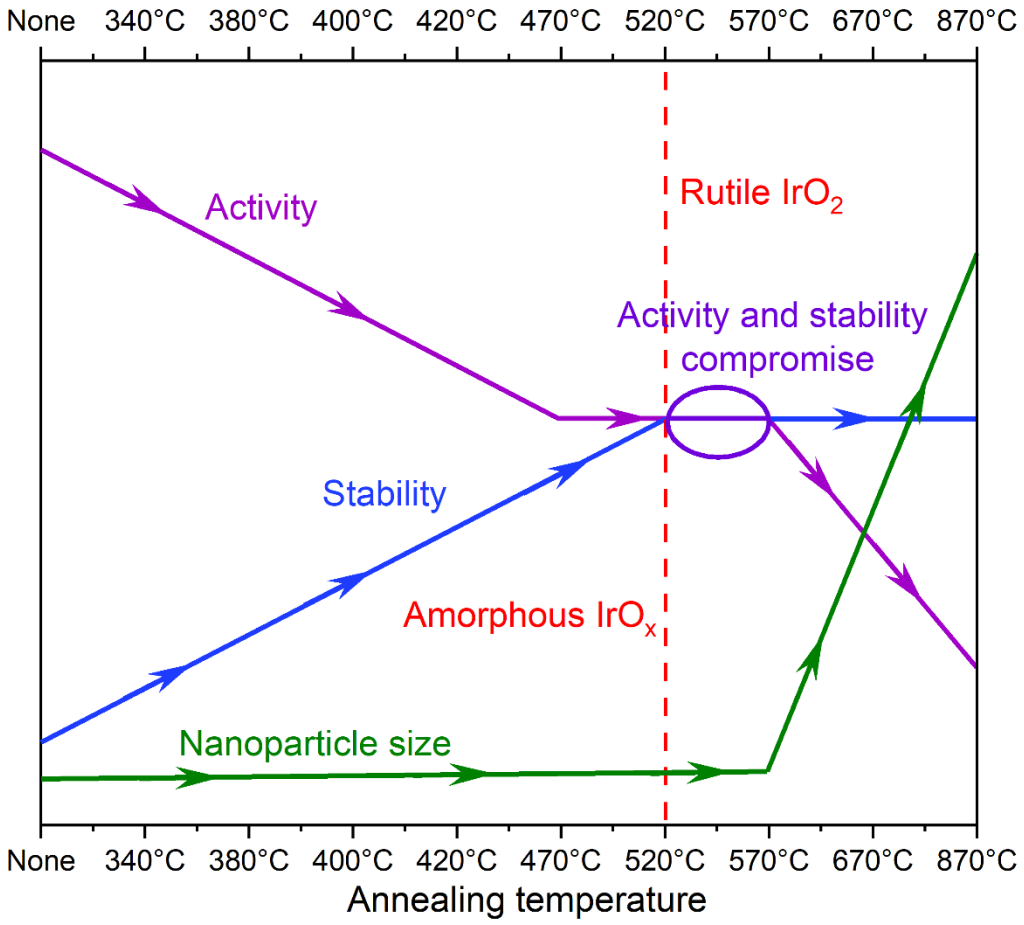

INTRODUCTION

The global energy demand is constantly rising, with over 80 % of the current energy consumption derived from fossil fuels contributing to climate change and environmental degradation. Hydrogen (H_2) offers a versatile and efficient energy solution for various sectors, including medium and heavy duty transportation and chemical and industrial processes.[1] However, currently, 96 % of the industrial H_2 production relies on fossil fuels.[2] One technology that stands out for the production of green H_2 is proton-exchange membrane water electrolysis (PEMWE). This technology enables the production of high-purity H_2 while operating at high pressures and high current density, and under dynamic operation conditions, making it easily compatible with renewable energies.[3,4] A key challenge in PEMWE electrocatalysis is enhancing the rate of the sluggish Oxygen Evolution Reaction (OER).[5] The conditions for the OER within a PEMWE are highly acidic and oxidative, which restricts the choice of catalysts to noble metal oxides.[6] For now, micrometric iridium oxide (IrO_x) is the state-of-the-art catalyst for the OER in PEMWE, thus requiring iridium (Ir) loading in the range of 1 mg cm^{-2}_{geo}. However, given the high cost and limited availability of Ir (0.02 ng g^{-1} in the earth crust[7] with an extraction of less than 10 t $year^{-1}$) coupled with increasing demand (7.4 t in 2023),[8] a drastic reduction in Ir loading is essential to enable widespread application of PEMWEs. To achieve the 2050 objective of reducing the Ir loading in PEMWE by a factor of 20,[9] one proposed solution is to use IrO_x nanoparticles (NPs). Indeed, by maximizing the surface-to-volume ratio, NPs achieve high electrocatalytic activity while minimizing the amount of metal needed.[10,11] However, the instability of high surface area carbon or metal oxide supports under acidic OER conditions raises concerns about the long-term viability of this approach. Daiane Ferreira da Silva *et al.*[11] recently compared the benefits and limitations of supported *vs.* unsupported IrO_x catalysts. They found that supported IrO_x NPs are more active

towards the OER but suffer from reduced stability compared to their unsupported counterparts, primarily due to the metal oxide support corrosion, which corroborates earlier findings by Claudel *et al*.[12] In contrast, unsupported IrO_x materials provide sustainable OER activity but are constrained by a lower density of catalytic sites and a reduced turnover frequency. Therefore, the development of self-supported small IrO_x NPs with a mesoporous structure is highly desirable.[13,14]

The self-supported IrO_x NPs must also balance OER activity and stability. Studies have shown that achieving this balance requires a high ratio of Ir(IV) to Ir(III) species and a large specific surface area.[15] One approach to reach this compromise is to subject the IrO_x catalysts to high-temperature thermal treatment, which promotes the formation of thermally stable rutile IrO_2 due to the strong Ir-O bonding energy.[16–18] Several studies have examined the influence of thermal treatment on the performance of OER electrocatalysts. Reier *et al*. focused on thin IrO_x films supported on titanium (Ti),[19] while Geiger *et al*. focused on porous thin films of hydrated IrO_x (HIROF).[20] In both cases, it was observed that the OER activity decreased with increasing thermal treatment temperature, while stability improved. It has been suggested that a temperature range of 400 to 500°C provides a good balance between activity and stability for HIROF catalysts, whereas an optimal range of 250 to 350°C was found for thin IrO_x films supported on Ti. Interestingly, high OER activity in both cases was associated with the presence of amorphous IrO_x, whereas high stability was linked to crystalline IrO_2. Karimi *et al*. investigated the effect of thermal treatment on IrO_x NPs synthesized using a polyol method and supported on antimony doped tin oxide (ATO).[21] They demonstrated that Ir oxy-hydroxide NPs transit from an amorphous structure to a crystalline one above 400°C. Additionally, they found that high-temperature thermal treatment leads to an increase in the NP size, resulting in a decrease in surface area, consistent with other literature studies.[22–24] Recently, Malinovic *et al*.[24] presented a synthesis of IrO_x NPs demonstrating

a good control over NP size during high-temperature thermal treatment using a silica encapsulation approach. However, removing the silica requires a solution of 1.68 % hydrofluoric acid in absolute ethanol, which raises concerns about environmental toxicity.

In this study, we introduce a model approach based on a sacrificial carbon support for synthesizing unsupported, small IrO_2 NPs with a mesoporous structure. Our method involves the synthesis of IrO_x/C NPs using a classical polyol method. During calcination in air at temperatures ranging from 340°C to 670°C, the IrO_x NPs aggregate and merge to form a randomly close-packed structure of IrO_x ($x \leq 2$) nanocrystallites (1-8 nm), with the carbon support serving as a sacrificial template. Using a combination of advanced Synchrotron and laboratory techniques, we demonstrate that the physical properties of the IrO_x mesoporous structure - including the Ir oxidation state, IrO_x crystallographic structure, and crystallite size - can be finely tuned by varying the calcination conditions. This in turn enables precise control over the OER activity and stability of the synthesized materials.

RESULTS AND DISCUSSION

Synthesis and Initial Morphology, Structure, and Chemical Composition of the material library

The IrO_x/C NPs were synthesized using a modified polyol synthesis.[25] Initially, an Ir salt ($H_2IrCl_6.xH_2O$, 99%, Alfa Aesar) is reduced in the presence of ethylene glycol (EG). This solution undergoes microwave heating to reflux under argon (Ar) atmosphere for 1 hour, yielding a colloidal solution of IrO_x NPs. Microwave heating was chosen for its ability to ensure uniform heating and to expedite the synthesis process. The NPs synthesized via both conventional and microwave heating exhibit comparable physical properties[26] (see **Figure S1**). Subsequently, a

support material (Vulcan® XC72) is introduced into the solution of IrO_x NPs to achieve a nominal weight fraction of *ca*. 20 wt. % Ir. The resultant IrO_x/C powder is then calcined at various temperatures under natural air convection using a tube furnace with a temperature ramp of a 1°C min^{-1} followed by a one hour hold at the target temperature. A schematic of this synthesis can be found in the **Figure S2**. A 1°C min^{-1} ramp was chosen to prevent the formation of metallic Ir during the annealing step. Indeed, we observed that, at high temperatures with a rapid heating ramp (8°C min^{-1}), the carbon support oxidizes releasing electrons that reduce the IrO_x NPs to metallic Ir NPs - a phenomenon known as carbo-reduction.[10] Although a 4°C min^{-1} ramp can mitigate this effect, using a slower heating ramp, coupled with a short hold at the target temperature, allows for the formation of smaller NPs, thus the choice of a temperature ramp of a 1°C min^{-1}. Before annealing the obtained NPs and to determine the temperatures relevant to our study, we conducted *in situ* X-ray diffraction (XRD) measurements of the IrO_x/C powder annealed in air within the range of 100°C to 700°C (see **Figure S3**). In total, ten catalysts were synthesized and characterized (IrO_x/C, IrO_x-340°C, IrO_x-380°C, IrO_x-400°C, IrO_x-420°C, IrO_x-470°C, IrO_x-520°C, IrO_x-570°C, IrO_x-670°C, IrO_x-870°C). The Ir weight fraction (wt. %), distribution of the IrO_x NPs on the Vulcan support, as well as the IrO_x particle size and shape were determined by Thermogravimetric Analysis (TGA) (see **Figure 1g**) and Transmission Electron Microscopy (TEM) under both *in situ* and *ex situ* conditions (see **Figure 1a** and **b)**, respectively. Particle size distributions (see **Figure 1h**) were determined using the ImageJ software based on the *ex situ* TEM images. The structural and chemical properties of the synthetized IrO_x NPs, including their degree of crystallinity, were assessed via XRD using both laboratory and Synchrotron sources (see **Figure 2a** and **b**, respectively), in conjunction with Pair Distribution Function (PDF) analysis, and the Ir oxidation state via X-ray Photoelectron Spectroscopy (XPS) (see **Figure 2d-f**). The IrO_x crystallite

size was also determined by PDF analysis, using the spherical particle approximation (see **Figure S4**). The size of the NPs closely matches that of the crystallites at high calcination temperature, indicating that the NPs are likely monocrystalline. Importantly, only isolated NPs were considered to build the NPs size distribution, leading to an underestimation at high temperature (larger NPs are often aggregated and were not considered to build the particle size distribution), as underlined by the comparison between NPs and crystallite size in the **Figure S4**. Moreover, the crystallite size determined from PDF analysis is significantly smaller than the NP size observed in TEM images at low calcination temperatures. This difference is expected, as the crystalline fraction is lower than the particle size, likely due to the amorphous nature of the NPs.

Figure 1 illustrates that, as the temperature increases, several phenomena occur simultaneously. The supporting carbon black gradually oxidizes into CO_2 and then completely disappears at around 470°C, leaving behind unsupported mesoporous IrO_2 NPs from 520°C onwards. This observation is supported by both *in situ* and *ex situ* TEM images (**Figure 1a** and **b,** respectively) and by TGA (**Figure 1g**). The initial weight loss, measured around 100°C, is attributed to the release of chemisorbed water. A second weight loss is observed between 300°C and 600°C, indicative of the combustion of the Vulcan carbon support. **Figure 1g** also shows that the pure Vulcan carbon requires heating to approximately 700°C for complete oxidation, whereas the Vulcan carbon support undergoes complete oxidation at a lower temperature range of 400–600°C. This difference is attributed to the catalytic effect of the IrO_x nanoparticles on the carbon oxidation reaction, confirming that carbon-based supports are unsuitable to support PEMWE anode catalysts. Finally, a weight gain is observed starting at around 900°C, which is attributed to the complete oxidation of IrO_x into IrO_2. This transformation is confirmed by the X-ray diffractogram of the powder after

TGA up to 1000°C, where only rutile IrO_2 is identified (see **Figure S5**). For samples IrO_x -520°C and above, no weight loss is detected between 300°C and 600°C, confirming that there is no carbon left in these samples. The Ir wt. % for each catalyst is detailed in the **Table S1**.

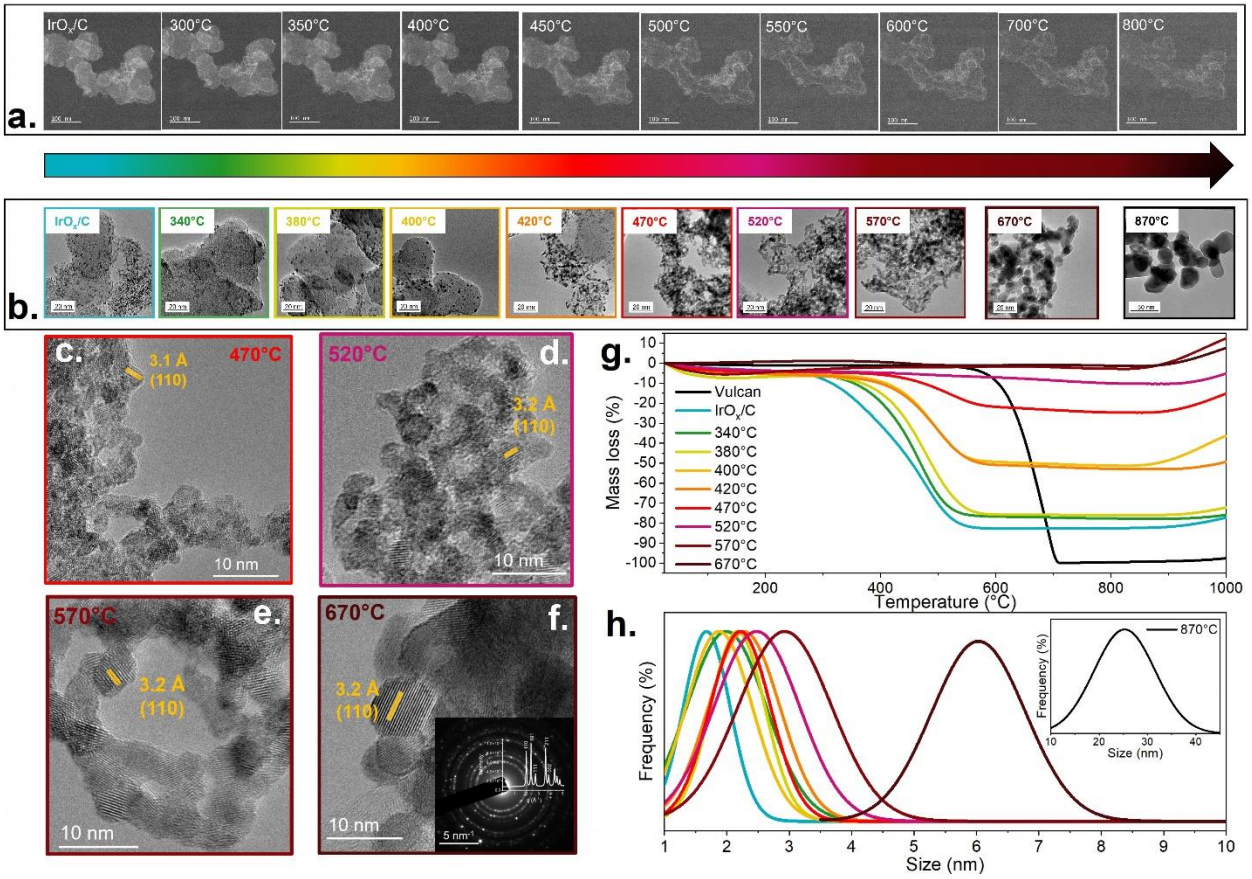

Figure 1 – (a) *In situ* high-angle annular dark field scanning transmission electron microscopy images of IrO_x/C catalysts, magnified 500 k times, being annealed between 100°C and 800°C employing a heating ramp of 4°C min^{-1} and maintaining each temperature for 7 min for TEM image acquisition. The atmosphere was a mixture of 50 % O_2 and 50 % Ar at 770 torr. (b) *Ex situ* TEM images, magnified 200 k times, of the ten catalysts of the material library. (c-f) *Ex situ* HR-TEM images of IrO_x catalysts subjected to thermal treatment at 470°C, 520°C, 570°C, 670°C, respectively and diffraction pattern of the IrO_x-670°C nanoparticles annotated with the experimental XRD pattern, highlighting the characteristic peaks of IrO_2 (inset). (g) Thermogravimetric analysis of the material library, and of Vulcan as a reference, conducted between 25°C and 1000°C at 5°C min^{-1} under air. (h) Particle size (diameter of the NP) distribution of the ten catalysts of the material library (IrO_x/C to 670°C in the main graph, and 870°C in the inset) evaluated from TEM images using ImageJ software.

In the initial IrO_x/C catalyst, the NPs have an average diameter of 1.7 ± 0.4 nm, and are homogenously distributed on the carbon support. As the temperature increases, the NP size increases (**Figure 1h** and **Figure S6**), reaching an average diameter of 6 ± 1 nm at 670°C. Notably, the NP size remains relatively small up to 570°C (2.9 ± 0.7 nm), with only a slight increase during

calcination. Unlike other studies that report a drastic increase in particle size above 500°C,[21,22] these results demonstrate the feasibility of obtaining small, unsupported IrO_x NPs even at high annealing temperature. Only when the temperature exceeds 800°C, larger NPs (25 ± 6 nm) with a broad size distribution are observed (see inset of **Figure 1h**), highlighting the optimal temperature range for achieving small IrO_x nanocrystallites.

The role of the Vulcan carbon support as a sacrificial template is better clarified by examining the *in situ* evolution of the IrO_x/C NPs during annealing. As shown in **Figure 1a**, **Figure S7** and **Figure S8**, the NPs deposited on the support maintain their positions on the carbon support even when annealed. Comparing the high-angle annular dark field scanning transmission electron microscopy (HAADF-STEM) images of the as-synthesized IrO_x/C with that of the same catalyst after annealing at 800°C reveals that the annealed IrO_x NPs follow the morphology of the pristine carbon particles/aggregates. However, they increase in size and aggregate to form an unsupported (confirmed by EDX analysis showing complete combustion of the carbon support at 800°C) IrO_x mesoporous structure composed of small interconnected NPs. **Figure S7** and **Figure S8** also show that the carbon support is initially calcined at the center of the particles before being fully corroded. This observation aligns with prior literature, which suggests that the center of carbon black particles is less structured than the outer periphery, and consequently, more prone to rapid oxidation.[27]

We now turn our attention to the structure and chemistry of the IrO_x NPs. The *ex situ* X-ray diffraction patterns (**Figure 2a**) indicate that IrO_x/C NPs are initially amorphous, and that the degree of crystallinity of the NPs increases as the calcination progresses, showing the characteristic peaks of tetragonal IrO_2 in XRD spectra from 520°C onwards. These results are in line with the *in situ* XRD measurements during the calcination of IrO_x/C from 100°C to 700°C, revealing the

appearance of crystalline IrO_2 phase between 400°C and 450°C (see **Figure S3**). The appearance of the rutile structure is also evidenced in the high resolution-TEM images (**Figure 1c-f**), where the interplanar distance can be determined by analyzing the atomic arrangement. Specifically, for IrO_x-470°C, IrO_x-520°C, IrO_x-570°C and IrO_x-670°C, the (110) lattice orientation of tetragonal IrO_2 was identified. Furthermore, a good correlation was found between the electron diffraction pattern of IrO_x-670°C and its experimental X-ray diffractogram, showing the characteristics peaks of tetragonal IrO_2 (see inset of **Figure 1f**).

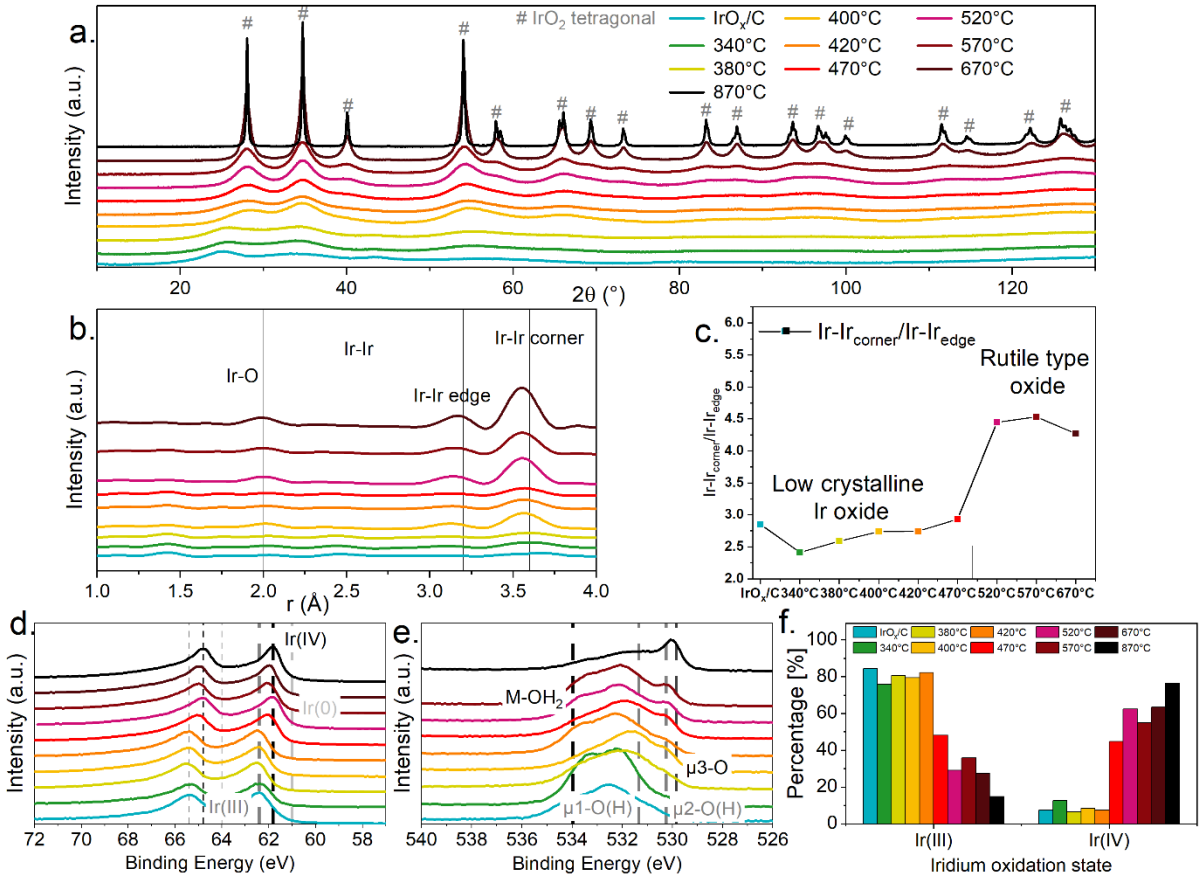

Figure 2 – (a) X-ray diffractograms obtained on IrO_x/C nanoparticles annealed at 340, 380, 400, 420, 470, 520, 570, 670 and 870°C in air. Each measurement lasted 13 minutes. The hashes correspond to tetragonal IrO_2 phase (PDF card 00-043-1019). (b) Short range pair distribution function analysis (0-4 Å) extracted from X-ray scattering data for the library of materials. The peak assignment was conducted according to the work of Pittkowski *et al.*[31] (c) Evolution of the ratio between Ir-Ir corner and Ir-Ir edge with the annealing temperature, illustrating the change in IrO_x crystallinity. X-ray photoelectron spectroscopy analysis of (d) Ir 4f core-level spectra and (e) O 1s core-level spectra of IrO_x nanoparticles. The position of the Ir(III), Ir(IV) and Ir(0) peaks are indicated in the Ir 4f region, and the position of M-OH_2, μ1-O(H), μ2-O(H) and μ3-O peaks are indicated in the O 1s region of the spectra. (f) Percentage of Ir(III) and Ir(IV) in each catalyst as a function of the annealing temperature, these percentages have been extracted from the XPS fits (see **Figure S9**).

An atomic pair distribution function (PDF) analysis was also conducted on the materials library. PDF analysis is a powerful technique that is widely used to study materials with no long-range order such as glasses and liquids.[28] In recent years, PDF analysis has developed into a powerful technique for gaining insights in the atomic structure of amorphous nanomaterials, particularly when conventional techniques fall short to the absence of long-range atomic order.[29,30] In essence, PDF analysis provides the weighted probability of finding a pair of atoms separated by a specific distance. The data obtained were fitted and adjusted using the methodology introduced by Pittkowski *et al*.[31] and Sun *et al*.[32] These fits were compared against reference models of metallic Ir, rutile IrO_2 and graphite. The PDF data can be found in the **Figure 2b** with a focus on the 0-4 Å part. The long-range PDFs extracted from X-ray total scattering data can be found in **Figure S9**. The disappearance of the peak at 1.4 Å, indicative of the C-C bond, between 470°C and 520°C, confirms the complete combustion of the Vulcan support above 470°C. Additionally, the abrupt increase in intensity of the two peaks at 3.2 Å and 3.6 Å, corresponding respectively to Ir-Ir bonds in edge-sharing and corner-sharing configurations between IrO_6 octahedra,[31] further confirms the change in crystallinity between 470°C and 520°C. The latter signs a transition in the material structure from a low crystalline Ir oxide to a rutile-type oxide, as depicted in **Figure 2c**.

To gain insights into the temperature-induced modifications of the near-surface chemical state of the IrO_x catalysts, XPS measurements were performed on the 10 samples from the materials library. The Ir 4f and the O 1s spectra are displayed in **Figure 2d** and **Figure 2e**, respectively. They were fitted using the methodology introduced by Freakley *et al*.,[33] already used in our group by Claudel *et al.*[12]. For the Ir 4f spectra, the contributions of Ir(0) (peaks at 60.8 eV and 63.8 eV), Ir(III) (peaks at 62.4 eV and 65.4 eV) and Ir(IV) (peaks at 61.8 eV and 64.8 eV) were considered.

A table summarizing the fitting parameters can be found in the Supporting Information (**Table S2**), along with the detailed fitted spectra for each sample (**Figure S10**). For the O 1s spectra, the methodology introduced by Roiron *et al.* was applied, considering the contributions of octahedral oxygen bridging Ir atoms, designated as μ3-O, as well as two types of defective oxygen with or without protonation μ1-O(H) and μ2-O(H).[34] Analysis of the Ir 4f spectra (**Figure 2d**) indicates that the samples do not present Ir(0) features, or if present, only in trace amounts. The as-synthesized IrO_x/C catalyst exhibits a mixed valence state of Ir(III) and Ir(IV), with Ir(III) being predominant. When the temperature increases, no discernable changes are observed until 470°C, where a shift towards lower binding energy becomes apparent, indicating an increase in the Ir(IV) content. This shift correlates with the sudden change in crystallinity between 470°C and 520°C, as discussed earlier. It also agrees with former literature reports indicating that changes in the oxidation state of Ir typically coincide with alterations in the crystallographic structure.[11] It is also interesting to note that changes in the Ir 4f correlate with those in the O 1s spectra. Between 470°C and 520°C, a shift towards lower binding energy is observed, culminating in a peak at 530 eV corresponding to lattice oxygen. This confirms the findings of Malinovic *et al*.,[24] who observed that the hydroxyl species present on the surface of IrO_x catalysts are progressively replaced by lattice oxygen when annealed at high temperature. The presence of a peak around 534 eV may be attributed to adsorbed water, possibly introduced during sample preparation;[24] however this assignment does not account for the peak's broadening at elevated temperatures. Previous studies have discussed the broadness of this peak. Peuckert[35] suggested that the broadening could be explained by the metallic electric conductivity of bulk IrO_2, which induces interactions between the valence band levels during the photoemission process, leading to kinetic energy losses of the photoelectrons. Da Silva *et al.*[36] attribute the peak at 533eV to metal-OH_2 bonds. Regardless of

the specific explanation, the broadening of this peak at high temperatures seems to be a fingerprint of a rutile IrO_2 phase. Finally, we emphasize that *ex situ* XPS measurements can serve as indicators of the catalyst's crystallinity and the presence of structural defects in the as-synthesized material [34]. However, they do not reflect the Ir oxidation state during the OER, where higher oxidation states than Ir(IV) have been observed through *in situ*/*operando* XAS studies, [37,38] and should ideally not be used to establish structure–chemistry–OER activity relationships.

A summary of the changes in morphology, structure and Ir oxidation state occurring during the annealing of IrO_x/C NPs is schematically presented in **Figure 3**. This summary highlights the complete combustion of the carbon support between 470°C and 520°C, the transition in crystallinity (from a mixture of low crystalline IrO_2 and IrO_x to highly crystalline IrO_2 NPs), and the change in Ir oxidation state (from predominantly Ir(III) at 420°C to a mixture of Ir(III)/Ir(IV) at 470°C to predominantly Ir(IV) at 520°C). Additionally, it shows that the size of the NPs can be kept below 3 nm up to 570°C, with NPs reaching approximately 6 nm at 670° C and 25 nm at 870°C. Importantly, at temperatures of 520°C and onwards, the catalysts show similar physico-chemical properties, with the only difference being the size of the NPs, offering an interesting platform to gain insights into the impact of NP size on OER activity.

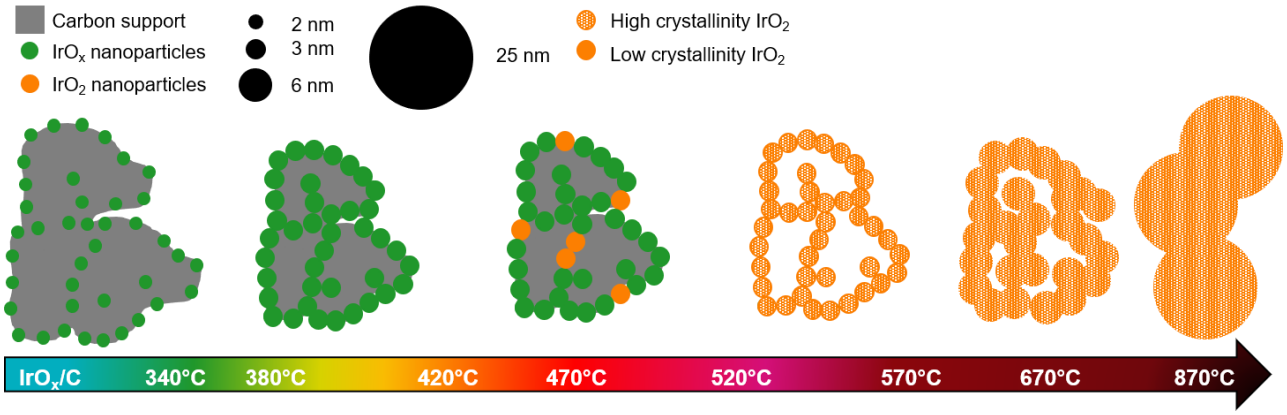

Figure 3 - Schematic picture illustrating the morphological, structural, and chemical changes of IrO_x/C nanoparticles occurring during annealing between 25 °C and 870 °C in air.

Relationships between the structure and the chemical composition of the IrO_x nanoparticles and their acidic OER activity

The unsupported small IrO_2 NPs from the materials library and a commercially available IrO_2 (99,99 %, Ir 84.5% min., Alfa Aesar, named IrO_2 comm. hereafter) were then used to establish the relationships between the catalyst's physico-chemical properties and their OER activity. The physico-chemical characterization (XPS, TEM and XRD) of IrO_2 comm. are presented in **Figure S10** and **Figure S11**, respectively.

The mass normalized cyclic voltammograms of three selected samples (IrO_x/C, IrO_x-470°C, and IrO_x-570°C) alongside with that of the benchmark IrO_2 comm. are presented in **Figure 4a-d**. A comparison of the mass normalized cyclic voltammograms for the entire materials library is provided in **Figure S12**. Two major observations emerge from this comparison. Firstly, the pseudocapacitive current decreases with increasing annealing temperature. This reduction in pseudocapacitive current can be associated with two phenomena: the increase in NP size, which results in a reduced surface over volume ratio ratio[1,7,10] and the decrease in the hydrous IrO_x content on the surface.[24,39] It could also have been associated with the decreasing carbon support surface area, but considering that the pseudocapacitive current of the carbon support is small, this contribution was considered negligible. Since the NP size changes only slightly until 570°C, it is reasonable to assume that the decrease in the hydrous IrO_x content present on the catalyst surface has a more significant influence, at least until 670°C. Secondly, the shape of the cyclic voltammograms changes with increasing annealing temperature. A redox couple around 0.95 V *vs*. the reversible hydrogen electrode (V_{RHE}), corresponding to the transition between Ir(III) and Ir(IV)[39,40] and thus indicative of the presence of Ir(III) in the (near) surface region of the IrO_x

catalyst, can be observed in the CV measured on the as-synthesized IrO_x/C NPs. The decrease in the electrical charge associated with this redox peak with increasing temperature aligns with the previously discussed increase of the Ir(IV) content in the catalysts (**Figure 2f**). The appearance of a new redox couple around 0.2 V_{RHE} at 520°C may be associated with the formation of a pseudo hydrogen underpotential deposition region (H_{UPD}), and thus indicative of the presence of metallic Ir (metallic Ir can adsorb hydrogen, similarly to platinum and rhodium).[41] This does not imply that metallic Ir appears during the annealing, but rather that the metallic surface, previously blocked by a hydrous oxide layer, would become accessible.[42] Another possible scenario could be hydrogen and ions insertion into the IrO_2 rutile structure.[43]

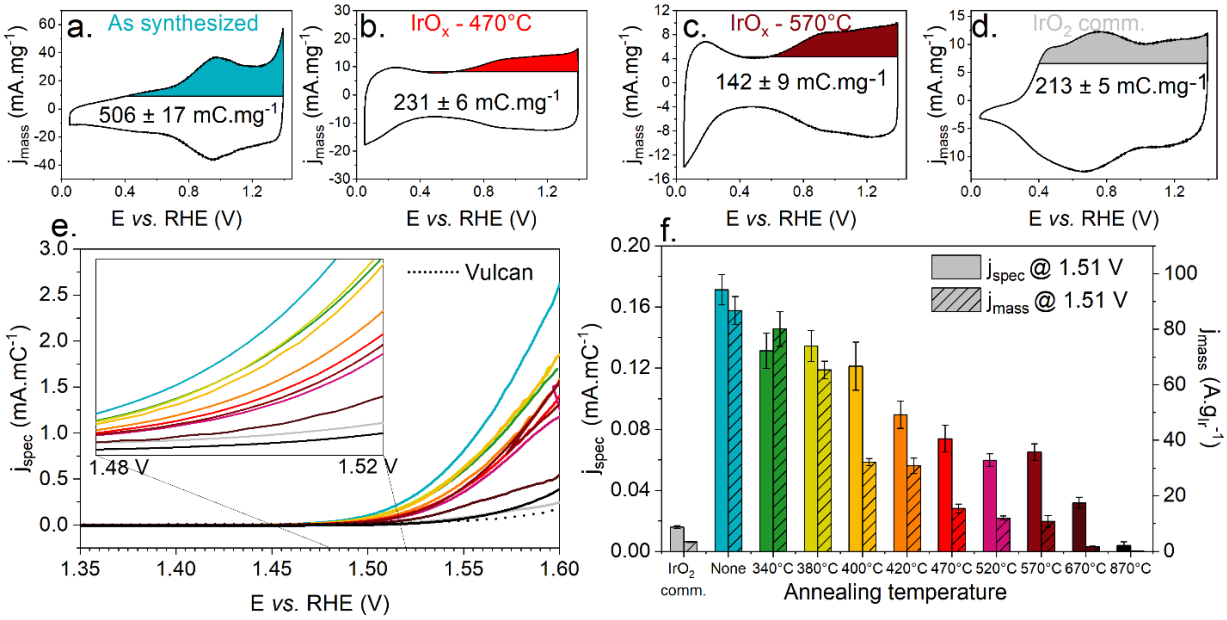

Figure 4 – (a-d) Mass normalized cyclic voltammograms measured at a scan rate of 50 mV s^{-1} of four selected samples, the last out of three cycles is presented. The calculated mass-normalized anodic charge recorded between 0.4 and 1.4 V_{RHE} is presented for each sample. (e) Charge normalized polarization curves (j_{spec}) extracted from linear sweep voltammograms between 1.2 and 1.6 V_{RHE}, with a potential sweep rate of 1 mV s^{-1} and forced convection of 2500 rpm. The inset corresponds to a zoom on the polarization curves between 1.48 V_{RHE} and 1.52 V_{RHE}, where the onset of the OER is observed. The polarization curves of Vulcan and of the benchmark IrO_2 comm. are presented for comparison. (f) Specific and mass activity for the OER measured at 1.51 V_{RHE} (onset of the OER) for the materials library and the benchmark IrO_2 comm. These OER activities have been determined from the polarization curves displayed in panel e). All rotating disk electrode measurements presented here have been done in de-aerated 0.1 M $HClO_4$ and 80 % of the Ohmic drop was dynamically compensated. The measurements were performed at least three times, and the average results are presented with error bars representing the standard deviation.

Figure 4e presents the OER specific activity of each sample, with Vulcan and IrO_2 comm. included for comparison. The specific activity was determined by normalizing the OER current to the anodic

charge recorded between 0.4 and 1.4 V_{RHE}, as extracted from the cyclic voltammograms shown in **Figure 4a-d**. This normalization method, widely used in the literature, accounts for the variation of the electrochemical active surface area (ECSA) with the NP size.[12,16,21,24] As the NP size increases, the surface-to-volume ratio ($\frac{S}{V} = \frac{4\pi r^2}{\frac{4}{3}\pi r^3} = \frac{3}{r}$, with r being the radius of the NP approximated as a sphere) decreases, leading to a reduction in ECSA. **Figure S13** shows a good correlation between the anodic charge recorded between 0.4 and 1.4 V_{RHE} and the surface-to-volume ratio $\frac{S}{V}$. **Figure 4f** displays the specific activity and the mass activity values at 1.51 V_{RHE} for each sample and the benchmark IrO_2. The mass activity towards the OER was determined by dividing the current by the mass of deposited Ir. The potential of 1.51 V_{RHE} was chosen because it is close to the OER onset. The specific and mass activity at 1.55 V_{RHE} can be found in **Figure S14**. The current densities at 1.55 V_{RHE} are more typical of those encountered in a PEMWE device (note that the Ir loading in a PEMWE anode is 100-200-fold larger). However, they include larger error bars due to the accumulation of oxygen bubbles.

Remarkably, the specific activity of the library of materials, except for IrO_x-870°C, surpasses that of the benchmark IrO_2 comm., by 8.5 times for the as synthesized IrO_x/C and by 3 times for IrO_x-670°C. Since the size of the NPs remains roughly the same from the as-synthesized IrO_x/C to the IrO_x-470°C catalyst (**Figure S4**), we attribute the changes in the initial OER activity to the decreasing fraction of Ir(III) species (decreasing Ir(III)/Ir(IV) ratio) present in the different catalysts (see the quantitative relationship between Ir(III)/Ir(IV) ratio and initial OER activity established by Claudel *et al.*[12]) and the associated change in crystallographic structure (amorphous IrO_x becomes rutile IrO_2). [11,19–22,24] In contrast, the IrO_x-570°C, IrO_x-670°C and IrO_x-870°C catalysts exhibit identical IrO_x chemistry and structure (see **Figure 2a** and **Figure 2d-f**), with a predominance of the Ir(IV) oxidation state and rutile structure, but have different NP sizes (see

Figure 1b and **Figure 1h**), as schematically represented on **Figure 3**. These variations in NP size lead to drastic changes in specific (and mass) OER activity. For instance, a 2.5-fold increase in NP size between 570°C and 670°C results in a 2-fold decrease in specific activity towards the OER. Similarly, a 3-fold increase in NP size between 670°C and 870°C leads to a 7.5-fold decrease in specific activity. Finally, we note no significant changes in specific and mass OER activity among IrO_x-470°C, IrO_x-520°C and IrO_x-570°C, despite their differing initial physico-chemical properties (see **Figure 3**). These observations suggest that, under OER conditions, the catalyst surface undergoes dynamical structural and chemical changes and that the chemistry and the structure of surface and near-surface region of similar IrO_x catalysts tend to converge towards a similar state, as previously proposed in the literature.[18,37,44] In turn, this could imply that the initial crystallography and Ir oxidation state have less impact on the initial OER activity compared to the size of the NPs (changing from 1.8 to 2.9 nm between 470 and 570°C). Testing in a membrane electrode assembly (MEA) configuration at elevated temperatures is however needed to confirm this hypothesis.

Relationships between the structure, the chemical composition and the stability of the different IrO_x materials

To ensure the reliability of a PEMWE system, an anode catalyst must maintain consistent electrocatalytic performance for tens of thousands of hours.[8] To gain quantitative insights into the balance between OER activity and stability, we conducted online ICP-MS measurements. This technique is widely used in the literature,[14,20,24,45] including by our group.[11,46,47] We measured the extent of Ir dissolution during a square wave accelerated stress test (AST) rather than galvanostatic or potentiostatic ASTs commonly used in literature. Indeed, potentiostatic or galvanostatic ASTs

often lead to the accumulation of oxygen bubbles on the surface of the electrode surface, making them less suitable for assessing the extent of degradation of OER catalysts.[48,49]

The measurement protocol is presented in **Figure 5a**, along with the real-time dissolution profile of IrO_x-470°C as an example. The measurement protocol consists of 5 steps. A conditioning step is first applied (100 CVs between 0.05 and 1.4 V_{RHE} at 500 mV s^{-1}), followed by a characterization step (3 CVs between 0.05 and 1.4 V_{RHE} at 5 mV s^{-1}). Next, a 45 min AST involving consecutive square wave (SQW) cycles of potential of 3 s each between 0 V_{RHE} and 1.51 V_{RHE} is applied. This AST simulates the electrochemical potentials that an anodic IrO_x catalyst may experience during unprotected start-stop events. The value of 1.51 V_{RHE} corresponds to the potential experienced by the anodic IrO_x catalysts at low OER current density in beginning-of-life conditions. Importantly, due to constraints in the online ICP-MS setup (specifically, the blockage of the catalyst's surface by O_2 bubbles at high current densities), it was not possible to accurately assess the stability of the synthesized IrO_x catalysts at higher potentials. Steps 1 and 2 are then repeated to assess the dynamic changes in the stability of the IrO_x catalysts over time. As shown in **Figure S15**, the intensity of the Ir dissolution peaks is significantly reduced after the AST, explaining why the stability of OER materials, as measured by on-line ICP-MS, often differs substantially from that assessed in MEA tests. [8,50,51] Strictly speaking, on-line ICP-MS measurements should be conducted until the catalyst reaches a steady-state dissolution regime. However, extending the AST duration may lead to oxygen bubbles poisoning (which reduces the density of the electrochemically active surface area leading to an artificial stabilized Ir dissolution rate), cause drift in ICP-MS measurements, and the time required to reach this state may vary depending on the robustness of the catalyst. To balance the Ir dissolution rate and experiment duration, we

calculated mass-normalized Ir dissolution values for each catalyst, including the benchmark IrO_2, over the 45-minute AST.

Figure 5b shows that the Ir concentration in solution decreases with rising annealing temperature, showing a significant drop between 470°C and 520°C, followed by a plateau from 520°C onwards, where the stability of the IrO_x catalysts becomes comparable to the benchmark IrO_2. This change in stability can be attributed to the transformation in the crystallographic structure and the presence of Ir atoms in a (IV) oxidation state above 500°C, in line with former literature findings.[17,19,20,24,52] The structural and chemical transformations are observed simultaneously, making it impossible to determine whether the chemistry or the structure governs the resistance to the dissolution of Ir atoms. Our results nevertheless suggest that annealing at a moderate temperature between 400 and 500°C will always be beneficial for the stability of an IrO_x-type material. We also calculated the stability number values of all catalysts ($S - number = \frac{n_{O_2(OER)}}{n_{Ir(dissolution)}}$)[16] during the 45 min. long AST (see **Figure S16**). The *S*-number values highlight a marked increase in stability between 470°C and 520°C, corresponding to the structural transition from amorphous IrO_x to rutile IrO_2. A decline in the S-number value is observed at temperatures above 520°C. This decrease is attributed to an increase in IrO_x particle size, from 2.9 ± 0.7 nm at 570°C to 6 ± 1 nm at 670°C and further to 25 ± 6 nm at 870°C, leading to a significant reduction in OER mass activity.

The high *S*-number value for IrO_x-520°C (2.8E+7 ± 0.2E+7) suggests that an annealing temperature of 520°C provides an optimal balance between OER activity and stability. This temperature is specific to the IrO_x/C system, as evidenced by the differing optimal temperatures reported in the literature for annealed IrO_x catalysts, which range between 250 and 500°C. [11,19–21] This can be easily rationalized as the optimal temperature results from the combined influence of

factors such as the temperature program (*e.g.*, heating rate, temperature hold, and hold duration) and oxygen concentration (*e.g.*, air flow, static air, or O_2 flow), as well as the distinct characteristics of the IrO_x materials used in different studies (*e.g.*, initial Ir oxidation state, crystallite size, and particle size). Despite these differences, our results confirm the ability to fine-tune thermal annealing conditions to oxidize Ir surface atoms effectively, achieving high stability while minimizing crystallite growth, thereby maintaining high OER mass activity.

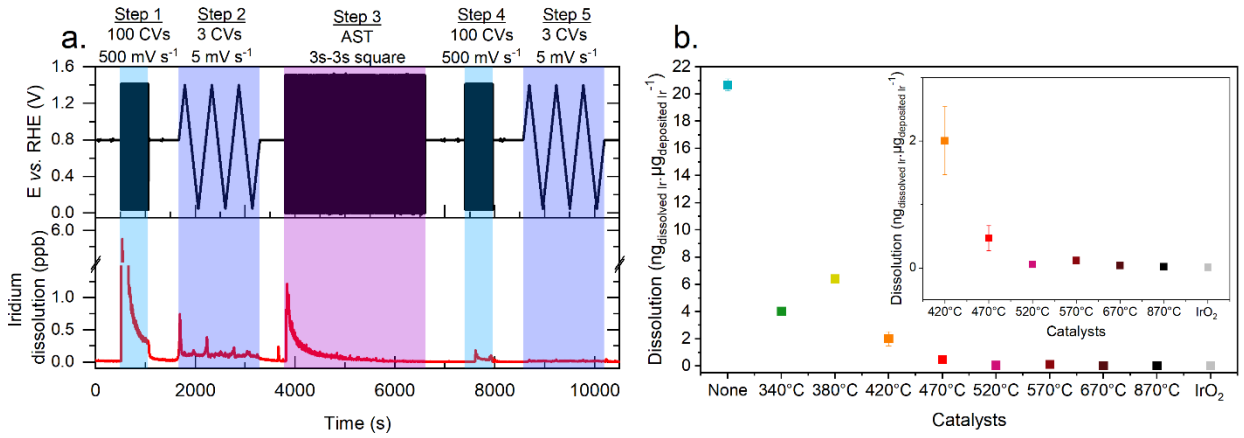

Figure 5 - (a) On-line Ir dissolution profile (example with IrO_x-470°C) during the stability assessment tests. These tests were performed in a flow cell with Ar-saturated 0.1 M $HClO_4$ electrolyte using an inductively-coupled plasma mass spectrometer ICP-MS that measures in real time the Ir concentration in solution. (b) Iridium dissolution ($ng_{dissolved\ Ir}.\mu g_{deposited\ Ir}^{-1}$) calculated for all the electrocatalysts during an AST (step 3 of the stability assessment measurements), comprised of square steps at 0 V_{RHE} for 3 s, followed by square step at 1.51 V_{RHE} for 3 s, all for a total duration of 45 min. The measurements have been done at least three times and the average results are presented, with the respective error bars.

CONCLUSION

In summary, we have presented a straightforward and easily reproducible synthesis method for producing mesoporous self-supported IrO_x NPs with excellent electrocatalytic properties for the acidic OER. Our method utilizes a sacrificial high-surface-area carbon support as a template during the annealing of IrO_x/C NPs. By carefully controlling the annealing temperature, we have designed a range of IrO_x nanomaterials with unique chemical and structural characteristics. Comprehensive physicochemical characterizations, including synchrotron X-ray diffraction and pair-distribution function analysis, revealed that thermal annealing promotes the crystallization of IrO_x into rutile

IrO_2 while simultaneously altering the oxidation state of the Ir atoms. These combined structural and chemical changes enhance the stability of the IrO_x materials, although they result in reduced OER activity, confirming previous literature findings. We found that an annealing temperature of 520°C offers the best balance between OER activity and stability, with Ir dissolution values leveling off beyond this temperature. Our study also shows that the initial structural properties play a crucial role in the stability of the IrO_x catalysts, with rutile IrO_2 exhibiting minimal Ir dissolution rate. The influence of IrO_x NP size was also highlighted, indicating that small IrO_2 NPs (< 3 nm) achieve a favorable balance between the OER activity and the stability.

MATERIALS AND METHODS

Material synthesis

The IrO_x/C NPs were synthesized using an adapted version of a polyol synthesis.[25,26] An Ir salt ($H_2IrCl_6.xH_2O$, 99%, Alfa Aesar) is first reduced in the presence of ethylene glycol (EG). Specifically, 34.512 g of a 6.95 g_{Ir} L^{-1} solution of this Ir salt in ultrapure water (UW) was added to a mixture of 480 mL of EG and 240 mL of UW, under magnetic stirring. The solution's pH was then adjusted to 12 by adding a 0.5 M NaOH solution in a 1:1 volume ratio of EG:UW. Subsequently, this solution was heated to reflux under Ar atmosphere for 1 hour using microwave heating, with a heating ramp of 10°C min^{-1}, resulting in a colloidal solution of IrO_x NPs. Following this, a support material was introduced to achieve a nominal mass fraction of 20 wt. % Ir. Specifically, 0.96 g of Vulcan XC72 (Cabot) was dispersed in 480 mL of a 1:1 volume ratio mixture of EG:UW. The pH was then adjusted to 2-3 by adding dropwise a 0.5 M H_2SO_4 solution in a 1:1 volume ratio mixture of EG:UW. After stirring at room temperature for 20 hours, IrO_x/C NPs were obtained, filtered, washed four times with UW, and finally dried at 95 °C overnight. The resulting powder was then calcined at various temperature under natural air convection using a tube furnace with a 1°C min^{-1} temperature ramp, followed by a 1 h hold at the aimed temperature. A schematic of this synthesis can be found in **Figure S2**. Ten catalysts with distinct structural and chemical properties were obtained: as synthesized IrO_x/C, IrO_x-340°C, IrO_x-380°C, IrO_x-400°C, IrO_x-420°C, IrO_x-470°C, IrO_x-520°C, IrO_x-570°C, IrO_x-670°C and IrO_x-870°C.

Electrochemical activity measurements

To assess the OER activity of the catalysts, a four-electrode electrochemical cell thermostated at 25°C was used. The working electrode consisted of a 5 mm diameter gold rotating disk electrode (RDE),[53,54] on which 10 µL of a catalyst suspension was deposited, as described by Claudel *et al.*.[12] Both the counter electrode and the fourth electrode are made of platinum. The reference

electrode is a reversible hydrogen electrode (RHE), and all potentials in this study are referred to the RHE (noted V_{RHE}). Prior to electrochemical measurements, all the glassware was rinsed using a 1:1 H_2SO_4:H_2O_2 solution overnight, then thoroughly washed with MQ-grade water. The electrolyte was a 0.1 M $HClO_4$ solution[55] which was prepared from 70 wt.% $HClO_4$ (Roth) and de-aerated with argon (Ar > 99.999 %, Messer) before each experiment.[56] In each experiment, the working electrode is introduced at a controlled potential of E = 0.8 V_{RHE}, and 100 cyclic voltammograms (CVs) are performed between 0.05 and 1.40 V_{RHE} at a scan rate of 500 mV s^{-1}. Subsequently, electrochemical impedance spectroscopy measurement is conducted to determine the high-frequency resistance of the cell. In subsequent experiments, 80% of this resistance value was dynamically compensated. Three CVs were performed between 0.05 and 1.40 V_{RHE} at a scan rate of 50 mVs^{-1} to determine the anodic charge between 0.4 and 1.40 V_{RHE} in the last cycle. Finally, a polarization curve was conducted between 1.20 and 1.60 V_{RHE} at a scan rate of 1 mV s^{-1}, with a RDE rotation of 2500 rpm to determine the electrocatalytic activity towards the oxygen evolution reaction.[57] The currents obtained at 1.51 V_{RHE} or 1.55 V_{RHE} were extracted from the polarization curves and subsequently normalized, either by the initial mass of Ir on the electrode to obtain mass activity towards the OER, denoted as j_{mass}, or by the anodic charge between 0.40 and 1.40 V_{RHE} to obtain the specific activity towards the OER, denoted as j_{spec}.

On-line inductively coupled plasma mass spectrometry measurements

To evaluate the stability of the nanocatalysts, we used an AST consisting of potential steps between 0 and 1.51 V_{RHE}, using a square-wave potential ramp (3 s at each potential), over a total duration of 45 min. This AST was conducted in an electrochemical flow cell with Ar-saturated 0.1 M $HClO_4$ as the electrolyte. This cell was coupled to an inductively coupled plasma mass spectrometer (NexION 2000c, PerkinElmer, Inc., Waltham, Massachusetts, USA), which analyzes the metal ion composition of the electrolyte in real-time after it passed through the flow cell. Calibration curves were prepared with standard solutions freshly obtained by dilution of a mono-element ICP standard solution (1000 mg L^{-1}, Carl Roth GmbH) with a 0.1 M HNO_3 solution. Before and after the AST, 100 CVs scans between 0.05 and 1.40 V_{RHE} at a scan rate of 500 mV s^{-1} and three CVs between 0.05 and 1.40 V_{RHE} at a scan rate of 50 mVs^{-1} were performed. The detailed measurement protocol is illustrated in **Figure 5**.

Thermogravimetric analysis

The Ir wt. % of each sample was determined through TGA, using a Mettler Toledo LF1100-XP1. 5 mg of sample was heated up to 1000°C in an air atmosphere with a temperature ramp of 5°C min^{-1}. The synthetic air flow rate was maintained at 200 mL min^{-1} throughout the annealing step. The calculated wt. % can be found in **Table S1**.

Transmission electron microcopy

All standard *ex situ* electron microscopy observations were carried out in a JEOL 2010 TEM operated at 200 kV (point-to-point resolution of 0.19 nm). The samples were prepared by depositing the NPs powder onto a lacey formvar carbon-supported copper grid (200 mesh Cu). The average mean particle size was measured using the ImageJ software. Only isolated particles were considered to build the particle size distribution, meaning that the TEM size (**Figure 1h** and **Figure S4**) represents the size of each grain, and not of the aggregates.

HR-TEM measurements and the *in situ* STEM observations in gas phase were conducted using a double aberration-corrected JEOL ARM 200F microscope equipped with a cold field emission gun operated at 200 k.

Environmental Scanning Transmission electron microcopy

For the *in situ* experiments, a Protochips Atmosphere TEM environmental high-pressure gas cell (HPGC) was utilized. This set-up consists of a pair of silicon microchips (called E-chips), which are aligned and assembled in closed-cell configuration at the tip of a dedicated TEM sample holder. The small E-chip is a 2 mm × 2 mm, 300 µm-thick silicon chip with a 300 µm × 300 µm, 50 nm-thick amorphous SiN window at its center. The large E-chip measures 6.0 mm × 4.5 mm and is 300 µm thick, with a 300 µm × 300 µm SiC membrane at its center. The SiC film is patterned with six circular windows, each 7 µm in diameter, arranged in two lines of three and composed of 30 nm thick amorphous SiN. The IrO_x/C sample was deposited on the large E-chip by drop casting 10 µL of a suspension of IrO_x/C NPs ultrasonically dispersed in ultrapure water. STEM observations were carried out through these electron-transparent windows. The IrO_x/C NPs were subjected to a mixture of 50% pure argon (Messer, purity > 99.999%) and 50% pure oxygen (Messer, purity > 99.999%) in static gas conditions using a manually-operated gas manifold from Protochips. The gas pressure in the high-performance gas cell was fixed to 770 torr and was controlled using an MKS PDR 2000 dual capacitance manometer. The sample was heated by resistive heating of the SiC membrane via current injection using an electronic control unit interfaced with Protochips Aduro 300 software with closed-loop temperature control. For temperature control, the software used chip-specific ohmic resistance of the SiC film versus temperature calibration files as input. The NPs were heated up to 800°C, with a heating ramp of 4°C min^{-1} (the desired heating ramp of 1°C min^{-1}) could not be achieved in this setup due to time constraints; however, no metallic Ir was detected). Images were acquired every 50°C, with a measuring time of approximately 7 minutes. The NPs were imaged in STEM mode using both high-angle annular dark field (HAADF) and bright field (BF) detectors. STEM images were acquired at magnifications of × 250 k (**Figure S7**) and × 500 k (**Figure 1a** and **Figure S8**). To limit the effect of the electron beam during *in situ* STEM imaging, no higher magnification was used and the electron was blanked between image acquisition.

Laboratory and Synchrotron X-ray Diffraction

The crystallinity of the samples was determined using X-ray diffraction measurements (XRD). These measurements were performed in θ-2θ mode on an X' Pert PRO MPD X-ray diffractometer using a Cu *K*α radiation source (λ = 0.15419 nm). The diffraction data were collected at a constant rate of 0.1° min^{-1} over an angle range of 2θ = 8-140 °.

Synchrotron Wide-Angle X-ray Scattering (WAXS) measurements were performed at the ID31 beamline of the European Synchrotron Radiation facility (ESRF) in Grenoble, France. The high energy X-ray beam (76 keV, λ = 0.16 Å) was focused on the catalyst powders in a capillary, and the scattered signal was collected using a Dectris Pilatus CdTe 2M detector positioned 298 mm behind the sample. The energy, detector distance and tilts were calibrated using a standard CeO_2 powder. A Pair Distribution Function analysis of the WAXS patterns was performed using the Fullprof software to extract the phase structure, crystallite size, lattice parameter using the $P4_2/mnm$ structure of IrO_2, the Fm-3m structure of metallic Ir and the graphite. The instrumental resolution function was determined by the refinement of a CeO_2 standard sample.

X-ray Photoelectron Spectroscopy

To determine the oxidation state of Ir, X-ray photoelectron spectroscopy analyses were performed using a Thermo Scientific *K*-alpha spectrometer with a monochromatized Al X-ray source ($h\nu = 1486.6$ eV; spot size = 400 µm). For each spectrum, C 1s, O 1s and Ir 4f regions were observed. The C 1s signal from adventitious carbon was utilized to calibrate the binding energy, set to a value of 285 eV. The obtained spectra were fitted using Thermo Scientific™ Advantage Software. The fit parameters and the fitted spectra can be found in **Table S2** and **Figure S10**.

AUTHOR INFORMATION

Corresponding Author

*To whom correspondence should be addressed. E-mail: (D.C): delphine.clauss@grenoble-inp.fr; (F.M) : mailto:frederic.maillard@grenoble-inp.fr

Author Contributions

DC: conceptualization, investigation, data analysis, writing – original draft, V.M.: XPS and on-line ICP-MS measurement, J.N.: *in situ* environmental gas and heating STEM and HR-STEM experiments, R.C. and P.B.: PDF data analysis, J.D. and M.M.: PDF data acquisition, L.D. and F.M.: conceptualization, methodology, writing – review and editing, funding acquisition, supervision.

The manuscript was written through contributions of all authors. All authors have given approval to the final version of the manuscript.

Funding Sources

This work was supported by “France 2030” government investment plan managed by the French National Research Agency, under the reference “ANR-22-PEHY-0011”, in the frame of the MATHYLDE project. The research also benefited from the characterization equipment of the Grenoble INP – CMTC platform supported by the Centre of Excellence of Multifunctional

Architectured Materials ‘‘CEMAM’’ (grant ANR-10-LABX-44-01) funded by the ‘‘Investments for the Future’’ Program

ASSOCIATED CONTENT

Supporting Information.

The Supporting Information is available free of charge via the Internet at http://pubs.acs.org. It comprises:

- X-ray diffractograms of IrO_x/C NPs synthesized using conventional and microwave heating;
- Schematic of IrO_x/C NPs synthesis;
- *In situ* X-ray diffractograms of IrO_x/C NPs recorded at 25°C, 100°C, 150°C, 200°C, 250°C, 300°C, 350°C, 400°C, 450°C, 500°C, 600°C, 700°C, and 800°C in air;
- Comparison between the sizes of IrO_x/C NPs and crystallites;
- X-ray diffractograms obtained on IrO_x/C nanoparticles after TGA up to 1000°C;
- Ir wt. % in the ten catalysts used in this study;
- TEM images of the ten catalysts synthesized;
- *In situ* HAADF-STEM images of IrO_x/C catalysts during annealing between 100°C and 800°C in a 50% O_2 and 50% Ar atmosphere;
- Pair distribution function analysis extracted from X-ray scattering data for the materials library;
- X-ray photoelectron spectra (Ir 4f band) of the materials library and the parameters used for fitting them;
- TEM images and X-ray diffractograms obtained on IrO_2 comm.;
- Mass normalized cyclic voltammograms of the materials library;

- Linear correlation between the anodic charge between 0.4 and 1.4 V_{RHE} and the surface over volume ratio of the NPs;
- Specific and mass activity for the OER measured at 1.55 V_{RHE} for the materials library and benchmark IrO_2;
- On-line Ir dissolution profile of IrO_x/C and IrO_x/C-670°C.
- *S*-number values calculated for all the electrocatalysts during the 45 min. AST

ACKNOWLEDGMENT

The authors acknowledge the CEA-METSA network for STEM and HRTEM measurements and the ESRF for synchrotron WAXS measurements at beamline ID 31 (Proposal ihch1717).

REFERENCES

(1) Armaroli, N.; Balzani, V. The Future of Energy Supply: Challenges and Opportunities. *Angew. Chem., Int. Ed.* **2007**, *46* (1–2), 52–66. https://doi.org/10.1002/anie.200602373.
(2) Penner, S. S. Steps toward the Hydrogen Economy. *Energy* **2006**, *31* (1), 33–43. https://doi.org/10.1016/j.energy.2004.04.060.
(3) Carmo, M.; Fritz, D. L.; Mergel, J.; Stolten, D. A Comprehensive Review on PEM Water Electrolysis. *Int. J. Hydrogen Energy* **2013**, *38* (12), 4901–4934. https://doi.org/10.1016/j.ijhydene.2013.01.151.
(4) Shiva Kumar, S.; Himabindu, V. Hydrogen Production by PEM Water Electrolysis – A Review. *Mater. Sci. Energy Technol.* **2019**, *2* (3), 442–454. https://doi.org/10.1016/j.mset.2019.03.002.
(5) Reier, T.; Oezaslan, M.; Strasser, P. Electrocatalytic Oxygen Evolution Reaction (OER) on Ru, Ir, and Pt Catalysts: A Comparative Study of Nanoparticles and Bulk Materials. *ACS Catal.* **2012**, *2* (8), 1765–1772. https://doi.org/10.1021/cs3003098.
(6) Cherevko, S.; Zeradjanin, A. R.; Topalov, A. A.; Kulyk, N.; Katsounaros, I.; Mayrhofer, K. J. J. Dissolution of Noble Metals during Oxygen Evolution in Acidic Media. *ChemCatChem* **2014**, *6* (8), 2219–2223. https://doi.org/10.1002/cctc.201402194.
(7) Burlakovs, J.; Vincevica-Gaile, Z.; Krievans, M.; Jani, Y.; Horttanainen, M.; Pehme, K.-M.; Dace, E.; Setyobudi, R. H.; Pilecka, J.; Denafas, G.; Grinfelde, I.; Bhatnagar, A.; Rud, V.; Rudovica, V.; Mersky, R. L.; Anne, O.; Kriipsalu, M.; Ozola-Davidane, R.; Tamm, T.; Klavins, M. Platinum Group Elements in Geosphere and Anthroposphere: Interplay among the Global Reserves, Urban Ores, Markets and Circular Economy. *Minerals* **2020**, *10* (6), 558. https://doi.org/10.3390/min10060558.
(8) Murawski, J.; Scott, S.; Rao, R.; Rigg, K.; Zalitis, C.; Stevens, J.; Sharman, J.; Hinds, G.; Stephens, I. E. L. Benchmarking Stability of IrO_x in Acidic Media under O_2 Evolution

Conditions: A Review. *Johnson Matthey Technology Review* **2023**. https://doi.org/10.1595/205651323X16848455435118.
(9) Clapp, M.; Zalitis, C. M.; Ryan, M. Perspectives on Current and Future Iridium Demand and Iridium Oxide Catalysts for PEM Water Electrolysis. *Catal. Today* **2023**, *420*, 114140. https://doi.org/10.1016/j.cattod.2023.114140.
(10) Elmaalouf, M.; Odziomek, M.; Duran, S.; Gayrard, M.; Bahri, M.; Tard, C.; Zitolo, A.; Lassalle-Kaiser, B.; Piquemal, J.-Y.; Ersen, O.; Boissière, C.; Sanchez, C.; Giraud, M.; Faustini, M.; Peron, J. The Origin of the High Electrochemical Activity of Pseudo-Amorphous Iridium Oxides. *Nat. Commun.* **2021**, *12* (1), 3935. https://doi.org/10.1038/s41467-021-24181-x.
(11) Daiane Ferreira da Silva, C.; Claudel, F.; Martin, V.; Chattot, R.; Abbou, S.; Kumar, K.; Jiménez-Morales, I.; Cavaliere, S.; Jones, D.; Rozière, J.; Solà-Hernandez, L.; Beauger, C.; Faustini, M.; Peron, J.; Gilles, B.; Encinas, T.; Piccolo, L.; Barros de Lima, F. H.; Dubau, L.; Maillard, F. Oxygen Evolution Reaction Activity and Stability Benchmarks for Supported and Unsupported IrO_x Electrocatalysts. *ACS Catal.* **2021**, *11* (7), 4107–4116. https://doi.org/10.1021/acscatal.0c04613.
(12) Claudel, F.; Dubau, L.; Berthomé, G.; Sola-Hernandez, L.; Beauger, C.; Piccolo, L.; Maillard, F. Degradation Mechanisms of Oxygen Evolution Reaction Electrocatalysts: A Combined Identical-Location Transmission Electron Microscopy and X-Ray Photoelectron Spectroscopy Study. *ACS Catal.* **2019**, *9* (5), 4688–4698. https://doi.org/10.1021/acscatal.9b00280.
(13) Pushkarev, A. S.; Pushkareva, I. V.; Bessarabov, D. G. Supported Ir-Based Oxygen Evolution Catalysts for Polymer Electrolyte Membrane Water Electrolysis: A Minireview. *Energy Fuels* **2022**, *36* (13), 6613–6625. https://doi.org/10.1021/acs.energyfuels.2c00951.
(14) Ledendecker, M.; Geiger, S.; Hengge, K.; Lim, J.; Cherevko, S.; Mingers, A. M.; Göhl, D.; Fortunato, G. V.; Jalalpoor, D.; Schüth, F.; Scheu, C.; Mayrhofer, K. J. J. Towards Maximized Utilization of Iridium for the Acidic Oxygen Evolution Reaction. *Nano. Res.* **2019**, *12* (9), 2275–2280. https://doi.org/10.1007/s12274-019-2383-y.
(15) Yu, H.; Danilovic, N.; Wang, Y.; Willis, W.; Poozhikunnath, A.; Bonville, L.; Capuano, C.; Ayers, K.; Maric, R. Nano-Size IrO_x Catalyst of High Activity and Stability in PEM Water Electrolyzer with Ultra-Low Iridium Loading. *Appl. Catal., B* **2018**, *239*, 133–146. https://doi.org/10.1016/j.apcatb.2018.07.064.
(16) Geiger, S.; Kasian, O.; Ledendecker, M.; Pizzutilo, E.; Mingers, A. M.; Fu, W. T.; Diaz-Morales, O.; Li, Z.; Oellers, T.; Fruchter, L.; Ludwig, A.; Mayrhofer, K. J. J.; Koper, M. T. M.; Cherevko, S. The Stability Number as a Metric for Electrocatalyst Stability Benchmarking. *Nat. Catal.* **2018**, *1* (7), 508–515. https://doi.org/10.1038/s41929-018-0085-6.
(17) Binninger, T.; Mohamed, R.; Waltar, K.; Fabbri, E.; Levecque, P.; Kötz, R.; Schmidt, T. J. Thermodynamic Explanation of the Universal Correlation between Oxygen Evolution Activity and Corrosion of Oxide Catalysts. *Sci. Rep.* **2015**, *5* (1), 12167. https://doi.org/10.1038/srep12167.
(18) Czioska, S.; Boubnov, A.; Escalera-López, D.; Geppert, J.; Zagalskaya, A.; Röse, P.; Saraçi, E.; Alexandrov, V.; Krewer, U.; Cherevko, S.; Grunwaldt, J.-D. Increased Ir–Ir Interaction in Iridium Oxide during the Oxygen Evolution Reaction at High Potentials Probed by *Operando* Spectroscopy. *ACS Catal.* **2021**, *11* (15), 10043–10057. https://doi.org/10.1021/acscatal.1c02074.

(19) Reier, T.; Teschner, D.; Lunkenbein, T.; Bergmann, A.; Selve, S.; Kraehnert, R.; Schlögl, R.; Strasser, P. Electrocatalytic Oxygen Evolution on Iridium Oxide: Uncovering Catalyst-Substrate Interactions and Active Iridium Oxide Species. *J. Electrochem. Soc.* **2014**, *161* (9), F876. https://doi.org/10.1149/2.0411409jes.
(20) Geiger, S.; Kasian, O.; Shrestha, B. R.; Mingers, A. M.; Mayrhofer, K. J. J.; Cherevko, S. Activity and Stability of Electrochemically and Thermally Treated Iridium for the Oxygen Evolution Reaction. *J. Electrochem. Soc.* **2016**, *163* (11), F3132. https://doi.org/10.1149/2.0181611jes.
(21) Karimi, F.; Bazylak, A.; Peppley, B. A. Effect of Calcination Temperature on the Morphological and Electrochemical Characteristics of Supported Iridium Hydroxyoxide Electrocatalysts for the PEM Electrolyzer Anode. *J. Electrochem. Soc.* **2017**, *164* (4), F464–F474. https://doi.org/10.1149/2.0111706jes.
(22) Abbott, D. F.; Lebedev, D.; Waltar, K.; Povia, M.; Nachtegaal, M.; Fabbri, E.; Copéret, C.; Schmidt, T. J. Iridium Oxide for the Oxygen Evolution Reaction: Correlation between Particle Size, Morphology, and the Surface Hydroxo Layer from *Operando* XAS. *Chem. Mater.* **2016**, *28* (18), 6591–6604. https://doi.org/10.1021/acs.chemmater.6b02625.
(23) Escalera-López, D.; Czioska, S.; Geppert, J.; Boubnov, A.; Röse, P.; Saraçi, E.; Krewer, U.; Grunwaldt, J.-D.; Cherevko, S. Phase- and Surface Composition-Dependent Electrochemical Stability of Ir-Ru Nanoparticles during Oxygen Evolution Reaction. *ACS Catal.* **2021**, *11* (15), 9300–9316. https://doi.org/10.1021/acscatal.1c01682.
(24) Malinovic, M.; Paciok, P.; Koh, E. S.; Geuß, M.; Choi, J.; Pfeifer, P.; Hofmann, J. P.; Göhl, D.; Heggen, M.; Cherevko, S.; Ledendecker, M. Size-Controlled Synthesis of IrO_2 Nanoparticles at High Temperatures for the Oxygen Evolution Reaction. *Adv. Energy Mater.* **2023**, 2301450. https://doi.org/10.1002/aenm.202301450.
(25) Fiévet, F.; Ammar-Merah, S.; Brayner, R.; Chau, F.; Giraud, M.; Mammeri, F.; Peron, J.; Piquemal, J.-Y.; Sicard, L.; Viau, G. The Polyol Process: A Unique Method for Easy Access to Metal Nanoparticles with Tailored Sizes, Shapes and Compositions. *Chem. Soc. Rev.* **2018**, *47* (14), 5187–5233. https://doi.org/10.1039/C7CS00777A.
(26) Karimi, F.; Peppley, B. A. Comparison of Conventional versus Microwave Heating for Polyol Synthesis of Supported Iridium Based Electrocatalyst for Polymer Electrolyte Membrane Water Electrolysis. *Int. J. Hydrogen Energy* **2017**, *42* (8), 5083–5094. https://doi.org/10.1016/j.ijhydene.2017.01.090.
(27) Kinoshita, K., *Carbon: Electrochemical and Physicochemical Properties*. John Wiley & Sons: New York, 1988; 533 pages
(28) Billinge, S. J. L.; Kanatzidis, M. G. Beyond Crystallography: The Study of Disorder, Nanocrystallinity and Crystallographically Challenged Materials with Pair Distribution Functions. *Chem. Commun.* **2004**, No. 7, 749–760. https://doi.org/10.1039/B309577K.
(29) Lindahl Christiansen, T.; R. Cooper, S.; Ø. Jensen, K. M. There's No Place like Real-Space: Elucidating Size-Dependent Atomic Structure of Nanomaterials Using Pair Distribution Function Analysis. *Nanoscale Adv.* **2020**, *2* (6), 2234–2254. https://doi.org/10.1039/D0NA00120A.
(30) Young, C. A.; Goodwin, A. L. Applications of Pair Distribution Function Methods to Contemporary Problems in Materials Chemistry. *J. Mater. Chem.* **2011**, *21* (18), 6464–6476. https://doi.org/10.1039/C0JM04415F.
(31) Pittkowski, R. K.; Punke, S.; Anker, A. S.; Bornet, A.; Magnard, N. P. L.; Schlegel, N.; Graversen, L. G.; Quinson, J.; Dworzak, A.; Oezaslan, M.; Kirkensgaard, J. J. K.; Mirolo, M.;

Drnec, J.; Arenz, M.; Jensen, K. M. Ø. Monitoring the Structural Changes in Iridium Nanoparticles during Oxygen Evolution Electrocatalysis with *Operando* X-Ray Total Scattering. *J. Am. Chem. Soc.* **2024**, *146* (40), 27517–27527. https://doi.org/10.1021/jacs.4c08149.

(32) Sun, W.; Wang, Z.; Zhou, Z.; Wu, Y.; Zaman, W. Q.; Tariq, M.; Cao, L.; Gong, X.; Yang, J. A Promising Engineering Strategy for Water Electro-Oxidation Iridate Catalysts via Coordination Distortion. *Chem. Commun.* **2019**, *55* (41), 5801–5804. https://doi.org/10.1039/C9CC02447F.

(33) Freakley, S. J.; Ruiz-Esquius, J.; Morgan, D. J. The X-Ray Photoelectron Spectra of Ir, IrO_2 and $IrCl_3$ Revisited. *Surf. and Interface Anal.* **2017**, *49* (8), 794–799. https://doi.org/10.1002/sia.6225.

(34) Roiron, C.; Wang, C.; Zenyuk, I. V.; Atanassov, P. Oxygen 1s X-Ray Photoelectron Spectra of Iridium Oxides as a Descriptor of the Amorphous–Rutile Character of the Surface. *J. Phys. Chem. Lett.* **2024**, 11217–11223. https://doi.org/10.1021/acs.jpclett.4c02616.

(35) Peuckert, M. XPS Study on Thermally and Electrochemically Prepared Oxidic Adlayers on Iridium. *Surface Science* **1984**, *144* (2), 451–464. https://doi.org/10.1016/0039-6028(84)90111-0.

(36) Da Silva, L. A.; Alves, V. A.; de Castro, S. C.; Boodts, J. F. C. XPS Study of the State of Iridium, Platinum, Titanium and Oxygen in Thermally Formed IrO_2+TiO_2+PtO_X Films. *Colloids Surf., A* **2000**, *170* (2), 119–126. https://doi.org/10.1016/S0927-7757(99)00535-X.

(37) Diklić, N.; Clark, A. H.; Herranz, J.; Aegerter, D.; Diercks, J. S.; Beard, A.; Saveleva, V. A.; Chauhan, P.; Nachtegaal, M.; Huthwelker, T.; Lebedev, D.; Kayser, P.; Alonso, J. A.; Copéret, C.; Schmidt, T. J. Surface Ir^{+5} Formation as a Universal Prerequisite for O_2 Evolution on Ir Oxides. *ACS Catal.* **2023**, *13* (16), 11069–11079. https://doi.org/10.1021/acscatal.3c01448.

(38) Liang, C.; Katayama, Y.; Tao, Y.; Morinaga, A.; Moss, B.; Celorrio, V.; Ryan, M.; Stephens, I. E. L.; Durrant, J. R.; Rao, R. R. Role of Electrolyte pH on Water Oxidation for Iridium Oxides. *J. Am. Chem. Soc.* **2024**, *146* (13), 8928–8938. https://doi.org/10.1021/jacs.3c12011.

(39) Cherevko, S.; Geiger, S.; Kasian, O.; Mingers, A.; Mayrhofer, K. J. J. Oxygen Evolution Activity and Stability of Iridium in Acidic Media. Part 2. – Electrochemically Grown Hydrous Iridium Oxide. *J. Electroanal.Chem.* **2016**, *774*, 102–110. https://doi.org/10.1016/j.jelechem.2016.05.015.

(40) Pavlovic, Z.; Ranjan, C.; Gao, Q.; van Gastel, M.; Schlögl, R. Probing the Structure of a Water-Oxidizing Anodic Iridium Oxide Catalyst Using Raman Spectroscopy. *ACS Catal.* **2016**, *6* (12), 8098–8105. https://doi.org/10.1021/acscatal.6b02343.

(41) Woods, R. Hydrogen Adsorption on Platinum, Iridium and Rhodium Electrodes at Reduced Temperatures and the Determination of Real Surface Area. *J. Electroanal. Chem. Interfacial Electrochem.* **1974**, *49* (2), 217–226. https://doi.org/10.1016/S0022-0728(74)80229-9.

(42) Cherevko, S.; Geiger, S.; Kasian, O.; Mingers, A.; Mayrhofer, K. J. J. Oxygen Evolution Activity and Stability of Iridium in Acidic Media. Part 1. – Metallic Iridium. *J. Electroanal. Chem.* **2016**, *773*, 69–78. https://doi.org/10.1016/j.jelechem.2016.04.033.

(43) Chabanier, C.; Guay, D. Activation and Hydrogen Absorption in Thermally Prepared RuO_2 and IrO_2. *J. Electroanal. Chem.* **2004**, *570* (1), 13–27. https://doi.org/10.1016/j.jelechem.2004.03.014.

(44) Saveleva, V. A.; Wang, L.; Teschner, D.; Jones, T.; Gago, A. S.; Friedrich, K. A.; Zafeiratos, S.; Schlögl, R.; Savinova, E. R. *Operando* Evidence for a Universal Oxygen Evolution Mechanism on Thermal and Electrochemical Iridium Oxides. *J. Phys. Chem. Lett.* **2018**, *9* (11), 3154–3160. https://doi.org/10.1021/acs.jpclett.8b00810.
(45) Grote, J.-P.; Zeradjanin, A. R.; Cherevko, S.; Mayrhofer, K. J. J. Coupling of a Scanning Flow Cell with Online Electrochemical Mass Spectrometry for Screening of Reaction Selectivity. *Rev. Sci. Instrum.* **2014**, *85* (10), 104101. https://doi.org/10.1063/1.4896755.
(46) Scohy, M.; Abbou, S.; Martin, V.; Gilles, B.; Sibert, E.; Dubau, L.; Maillard, F. Probing Surface Oxide Formation and Dissolution on/of Ir Single Crystals via X-Ray Photoelectron Spectroscopy and Inductively Coupled Plasma Mass Spectrometry. *ACS Catal.* **2019**, *9* (11), 9859–9869. https://doi.org/10.1021/acscatal.9b02988.
(47) Abbou, S.; Chattot, R.; Martin, V.; Claudel, F.; Solà-Hernandez, L.; Beauger, C.; Dubau, L.; Maillard, F. Manipulating the Corrosion Resistance of SnO_2 Aerogels through Doping for Efficient and Durable Oxygen Evolution Reaction Electrocatalysis in Acidic Media. *ACS Catal.* **2020**, *10* (13), 7283–7294. https://doi.org/10.1021/acscatal.0c01084.
(48) El-Sayed, H. A.; Weiß, A.; Olbrich, L. F.; Putro, G. P.; Gasteiger, H. A. OER Catalyst Stability Investigation Using RDE Technique: A Stability Measure or an Artifact? *J. Electrochem. Soc.* **2019**, *166* (8), F458. https://doi.org/10.1149/2.0301908jes.
(49) Suermann, M.; Bensmann, B.; Hanke-Rauschenbach, R. Degradation of Proton Exchange Membrane (PEM) Water Electrolysis Cells: Looking Beyond the Cell Voltage Increase. *J. Electrochem. Soc.* **2019**, *166* (10), F645. https://doi.org/10.1149/2.1451910jes.
(50) Tovini, M. F.; Hartig-Weiß, A.; Gasteiger, H. A.; El-Sayed, H. A. The Discrepancy in Oxygen Evolution Reaction Catalyst Lifetime Explained: RDE *vs* MEA - Dynamicity within the Catalyst Layer Matters. *J. Electrochem. Soc.* **2021**, *168* (1), 014512. https://doi.org/10.1149/1945-7111/abdcc9.
(51) Ehelebe, K.; Escalera-López, D.; Cherevko, S. Limitations of Aqueous Model Systems in the Stability Assessment of Electrocatalysts for Oxygen Reactions in Fuel Cell and Electrolyzers. *Curr. Opin. Electrochem.* **2021**, *29*, 100832. https://doi.org/10.1016/j.coelec.2021.100832.
(52) Cherevko, S.; Reier, T.; Zeradjanin, A. R.; Pawolek, Z.; Strasser, P.; Mayrhofer, K. J. J. Stability of Nanostructured Iridium Oxide Electrocatalysts during Oxygen Evolution Reaction in Acidic Environment. *Electrochem. Commun.* **2014**, *48*, 81–85. https://doi.org/10.1016/j.elecom.2014.08.027.
(53) Yi, Y.; Weinberg, G.; Prenzel, M.; Greiner, M.; Heumann, S.; Becker, S.; Schlögl, R. Electrochemical Corrosion of a Glassy Carbon Electrode. *Catal. Today* **2017**, *295*, 32–40. https://doi.org/10.1016/j.cattod.2017.07.013.
(54) Edgington, J.; Deberghes, A.; Seitz, L. C. Glassy Carbon Substrate Oxidation Effects on Electrode Stability for Oxygen Evolution Reaction Catalysis Stability Benchmarking. *ACS Appl. Energy Mater.* **2022**, *5* (10), 12206–12218. https://doi.org/10.1021/acsaem.2c01690.
(55) Arminio-Ravelo, J. A.; Jensen, A. W.; Jensen, K. D.; Quinson, J.; Escudero-Escribano, M. Electrolyte Effects on the Electrocatalytic Performance of Iridium-Based Nanoparticles for Oxygen Evolution in Rotating Disc Electrodes. *ChemPhysChem* **2019**, *20* (22), 2956–2963. https://doi.org/10.1002/cphc.201900902.
(56) Garcia, A. C.; Koper, M. T. M. Effect of Saturating the Electrolyte with Oxygen on the Activity for the Oxygen Evolution Reaction. *ACS Catal.* **2018**, *8* (10), 9359–9363. https://doi.org/10.1021/acscatal.8b01447.

(57) Ioroi, T.; Nagai, T.; Siroma, Z.; Yasuda, K. Effect of Rotating Disk Electrode Conditions on Oxygen Evolution Reaction Activity of Ir Nanoparticle Catalysts and Comparison with Membrane and Electrode Assemblies. *Int. J. Hydrogen Energy* **2022**, S036031992204174X. https://doi.org/10.1016/j.ijhydene.2022.09.059.